Contribution of the myosin VI tail domain to processive stepping and intramolecular tension sensing

Alexander R. Dunn[a,1,3], Peiying Chuan[a,1], Zev Bryant[b], and James A. Spudich[a,2]

[a]Department of Biochemistry and [b]Department of Bioengineering, Stanford University School of Medicine, Stanford, CA 94305

Contributed by James A. Spudich, March 11, 2010 (sent for review December 3, 2009)

Myosin VI is proposed to act as both a molecular transporter and as an anchor in vivo. A portion of the molecule *C*-terminal to the canonical lever arm, termed the medial tail (MT), has been proposed to act as either a lever arm extension or as a dimerization motif. We describe constructs in which the MT is interrupted by a glycine-rich molecular swivel. Disruption of the MT results in decreased processive run lengths measured using single-molecule fluorescence microscopy and a decreased step size under applied load as measured in an optical trap. We used single-molecule gold nanoparticle tracking and optical trapping to examine the mechanism of coordination between the heads of dimeric myosin VI. We detect two rate-limiting kinetic processes at low (<200 micromolar) ATP concentrations. Our data can be explained by a model in which intramolecular tension greatly increases the affinity of the lead head for ADP, likely by slowing ADP release from the lead head. This mechanism likely increases both the motor's processivity and its ability to act as an anchor under physiological conditions.

gating | myo6 | TIRF | tweezers | gold nanoparticle tracking

Myosin VI uses the energy derived from ATP hydrolysis to transport cargo toward the minus end of actin filaments, the opposite direction as compared to other characterized myosins (1–3). In addition to its biological roles as a transporter in endocytosis (4–11) myosin VI is known to play important roles in normal and cancerous cell migration (12–14) and in the structural maintenance of the golgi apparatus (15, 16), microvilli (17, 18), and inner-ear stereocilia (19, 20). These results have led to the hypothesis that myosin VI additionally functions to shape and anchor cellular substructures within the actin cytoskeleton (21).

The myosin VI protein sequence *C*-terminal to the catalytic domain consists of two calmodulin-binding regions, a small, globular domain (proximal tail, PT), a structurally rigid, stable single α-helix termed the medial tail (MT), and a globular cargo binding domain (Fig. 1*A*) (22). The MT extends the lever arm by ∼10 nm in single-headed constructs, resulting in a lever arm swing of 30 nm (23). However, other recent results suggest that the proximal part of the MT may act as a dimerization motif, and that the PT instead unfolds to provide the reach necessary for the observed ∼30 nm steps of dimeric myosin VI constructs (24).

The kinetic mechanism underlying processive stepping by dimeric myosin VI is likewise poorly understood. Previous results were interpreted to support models in which the catalytic cycles of the front and rear heads of dimeric myosin VI are coordinated. This coordination could in principle occur by either blocking ADP release from or ATP binding (25) to the lead head.

We reasoned that if the MT acts as a lever arm extension its structural disruption should decrease the observed step size under applied load. We additionally examined the kinetic mechanism underlying processive stepping in both constructs with and without the swivel sequence in order to probe the contribution of the MT to intrahead coordination. Our data suggest that the MT contributes structurally to the stride of dimeric myosin VI, and that intramolecular tension blocks ADP release in the front head of processively stepping myosin VI dimers.

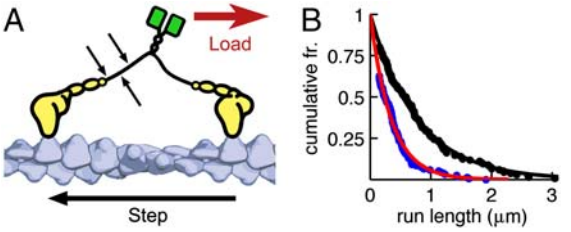

Fig. 1. (*A*) Dimeric myosin VI (M6) with and without swivels in the MT domain moves processively on actin (*Blue*). The *N*-terminal catalytic domain, bound calmodulins, and proximal tail (PT) domain are shown in yellow. The PT is followed by the medial tail (MT, *Black*), a GCN4 coiled-coil domain (*Black*), and a *C*-terminal YFP that replaces the cargo binding domain (*Green*). Three different constructs, swivel 1, 2, and 3, contain the amino acid sequence GGSGGSGGSGG inserted after residues L914, Q931, and R941 (*Small Arrows*), interrupting the MT. (*B*) Both control M6 dimer (referred to throughout as M6dimer; *Black*) and swivel 1 (*Blue*, fit in *Red*) move processively on actin. Run lengths of 780 ± 80 nm (M6dimer; $N = 113$) and 350 ± 30 nm (swivel 1; $N = 97$) were measured using single-molecule TIRF microscopy. Run lengths for the other swivel constructs are in Table 1.

Results

Inclusion of the Swivel Sequence Disrupts the MT. Inclusion of a swivel in the proximal region of the MT decreases the stroke size of a single-headed form of a swivel construct to 20 ± 1 nm, confirming that the swivel sequence disrupts local helicity (Fig. S1). The wild-type dimeric construct, referred to here as the M6dimer, is the same as that used in most previous studies (21); it is a dimer created by the inclusion of a GCN4 sequence near the *C* terminus after residue Arg^{992}.

Disruption of the MT Alters Processivity But Not Step Size Under ∼Zero Load. We used total internal reflection fluorescence microscopy (TIRF) (26) and gold nanoparticle tracking (GNT) to observe dimeric swivel constructs stepping processively along actin (27). Single-molecule TIRF observations demonstrate that all three dimeric swivel constructs (GGSGGSGGSGG inserted at residues Leu^{914}, Gln^{931}, and Arg^{941}) are processive but with run lengths that decrease as the swivel position is moved closer to the

Author contributions: A.R.D., P.C., Z.B., and J.A.S. designed research; A.R.D. and P.C. performed research; A.R.D., P.C., and Z.B. contributed new reagents/analytic tools; A.R.D., P.C., Z.B., and J.A.S. analyzed data; and A.R.D., P.C., Z.B., and J.A.S. wrote the paper.

No author conflict of interest response is available.

[1]A.R.D. and P.C. contributed equally to this work.

[2]To whom correspondence should be addressed. E-mail: jspudich@stanford.edu.

[3]Present address: Department of Chemical Engineering, Stanford University, Stanford, CA 94305.

This article contains supporting information online at www.pnas.org/cgi/content/full/1002430107/DCSupplemental.

www.pnas.org/cgi/doi/10.1073/pnas.1002430107

Table 1. Run lengths, velocities, and step sizes of dimeric myosin VI constructs measured under zero applied load

Construct	smTIRF run length (nm)	smTIRF velocity (nm s^{-1})	GNT forward step size (nm)	GNT fraction back steps
Swivel 1	350 (350) ± 30 ($N = 97$)*	31 ± 1*	30 ± 1† ($N = 222$)	16%†
	200 (240) ± 30 ($N = 75$)‡	114 ± 6‡		
Swivel 2	450 (470) ± 40 ($N = 118$)*	45 ± 1*	35 ± 1† ($N = 258$)	8%†
Swivel 3	530 (590) ± 50 ($N = 142$)*	39 ± 1*	33 ± 1† ($N = 277$)	6%†
M6dimer	780 (770) ± 80 ($N = 113$)*	45 ± 1*	34 ± 1§ ($N = 368$)	1%§
	440 (450) ± 50 ($N = 84$)‡	148 ± 6‡	34 ± 1‡ ($N = 196$)	3%‡

Run length and error determined by a bootstrap fit to single exponential. Maximum likelihood estimate (MLE) is shown in parentheses. Uncertainties for velocity and step size are SEM. GNT: gold nanoparticle tracking. Conditions:
*100 μM ATP.
†200 μM ATP.
‡2 mM ATP.
§120 μM ATP.

PT (Fig. 1*B* and Table 1). Higher temporal and spatial resolutions than those provided by TIRF microscopy are necessary to elucidate the stepping mechanism for both M6dimer and the swivel constructs. We therefore used GNT, which enables nanometer-resolution tracking at ∼1,000 times higher frame rates than single fluorophore imaging (28). We used evanescence darkfield microscopy (29) to image gold particles functionalized with single myosin VI molecules as they moved along surface-immobilized actin (Fig. 2*A* and Fig. S2). Total internal reflection (TIR) illumination markedly decreased background from out-of-focus particles (30), allowing us to work at higher particle concentrations than in previous experiments (27).

Step size and dwell time distributions for M6dimer are in good agreement with previously reported data, demonstrating that the attachment of the gold particle does not perturb stepping (Figs. S3 and S4) (31–37). All three swivel constructs take forward steps of between 30 and 34 nm in the GNT assay, nearly indistinguishable in size from those of M6dimer (Fig. 2*B* and Fig. S3 and Table 1). This observation is surprising given that the inclusion of the swivel disrupts the lever arm. However, our data are similar to observations made with a myosin V construct containing flexible breaks in its lever arm. This myosin V construct takes processive steps similar in size to those produced by control constructs (38). It is possible that structural constraints imposed by actin favor ∼30 nm steps for both myosin V and VI even in the presence of flexible lever arms.

Individual steps for both M6dimer and the swivel constructs are rapid (Fig. 2*C*). In the absence of an observable diffusive substep, we infer that the timescale for rebinding of the front head is fast (>200 s^{-1}), consistent with rebinding rates measured for myosin V, a processive plus-end directed motor (27). These free head rebinding rates are fast relative to the rate of the weak-to-strong binding transition in the new lead head (reported as ∼40 s^{-1}) (25), which should help the swivel constructs to maintain a high duty ratio and hence processive stepping.

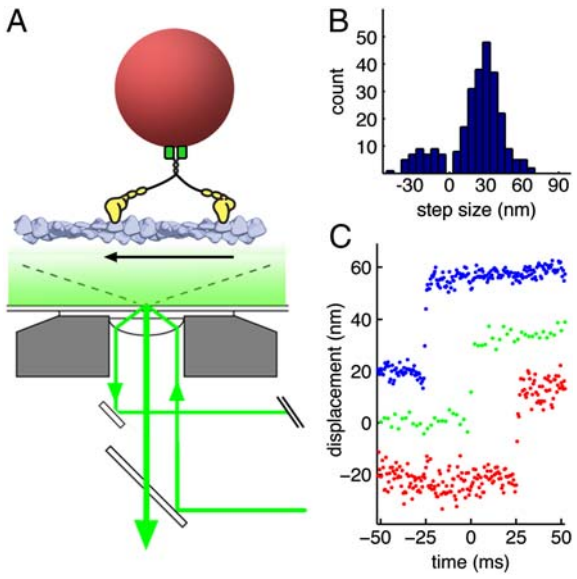

Fig. 2. (*A*) GNT schematic. M6dimer walks along surface-immobilized actin. Light from a 532 nm laser is totally internally reflected at the glass-water interface, creating evanescent illumination of the sample. The return beam is deflected by a small wedge mirror. Light scattered by gold particles (*Thick Beam*) passes through a 50/50 beam splitter and is imaged using a fast camera. (*B*) Dimeric swivel 1 takes large steps. A forward step size of 30 ± 1 nm (SEM, $N = 222$) was measured using gold nanoparticle tracking (GNT). (*C*) Averaged steps for M6dimer (*Blue*; 2,000 frames s^{-1}; $N = 93$), swivel 1 (*Green*, 500 frames s^{-1}; $N = 60$), and swivel 2 (*Red*, 2,000 frames s^{-1}; $N = 46$). Displacements due to the lever arm swing and the diffusive search occur faster than the time resolution of our measurement. Only steps with amplitudes between 30 and 45 nm are included in the above averages. These steps are expected to have substantial diffusive components in the case of the swivel constructs, which have stroke sizes measured at ∼20 nm.

Disruption of the Medial Tail Alters Step Size of the Dimeric Constructs Under Applied Load. We next used a single-molecule optical trap assay to assess the stepping behavior of the dimeric swivel constructs under a constant load. In contrast to M6dimer, the swivel 1 step size decreases rapidly with applied load (Fig. 3) (21). Extrapolation to zero force gives a predicted step size of 32 nm, in excellent agreement with the forward step size measured with GNT. These data demonstrate a clear difference between swivel 1 and M6dimer: The stiff MT in the M6dimer allows the motor to take large steps, even against appreciable backward load. These results are analogous to previous calculations of step sizes for theoretical models of myosin V (39), in which it was found that a lever arm bending rigidity of at least 1,000 pN nm^2 was required

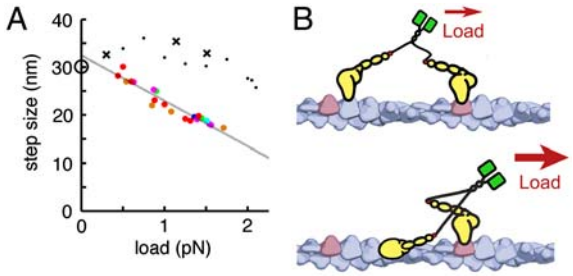

Fig. 3. The dimeric swivel 1 step size decreases under load. (*A*) Optical trapping with force-feedback was used to apply a constant load to processively stepping dimeric swivel 1. Each color represents a different molecule. An open circle indicates the step size at zero applied load as measured using GNT. A gray line shows a linear fit to the optical trap data. M6dimer step size data are indicated with a black ×. M6dimer step size data from ref. 21 are shown as black closed circles. (*B*) (*Top*) Under very low applied load the swivel 1 step size approximates the actin pseudohelical repeat (*Purple*). (*Bottom*) Higher loads result in decreased step size.

in order to maintain large step sizes under load, with the difference that in our case flexibility likely stems from a single flexible linker.

Dimeric Myosin VI Exhibits Multiple Kinetic Steps at Rate-Limiting ATP Concentrations. The hypothesized roles of myosin VI in cargo transport and anchoring would likely be enhanced by mechanisms that prevent premature detachment from actin. In myosin V, intramolecular strain slows ADP release from the front head, thus inhibiting ATP-mediated detachment from actin (40, 41). We sought to determine whether a similar mechanism, termed ADP gating, is also part of the myosin VI stepping mechanism.

If intramolecular tension sensing significantly increases the affinity of the lead head for ADP, the observed dwell time distribution will follow a sequential exponential model in which ADP must leave the rear head before ATP can bind (Fig. 4*A*). In contrast, if ADP gating is absent (unaltered lead head ADP binding and release kinetics), ADP would leave the front head at ~5 s^{-1} (2, 21, 35). In the latter case, if the stepping rate is sufficiently slow (in the presence of <250 μM ATP) ADP is likely to leave the front head before the next step occurs, resulting in a new trailing head that is devoid of ADP (Fig. 4*B*). In this second scenario the single rate-limiting step would be ATP binding, resulting in a single-exponential dwell time distribution.

The distribution of waiting times between steps for M6dimer in either the presence or absence of applied load and ~100 μM ATP is well-fit by a model containing two sequential processes (Fig. 4 and Tables S1 and S2). The slow and fast rates are consistent with previous measurements of ATP binding and ADP release at this ATP concentration (21). Because the stepping rates under these conditions are considerably slower than the rate of ADP release, we infer that ADP remains bound to the front head prior to the step.

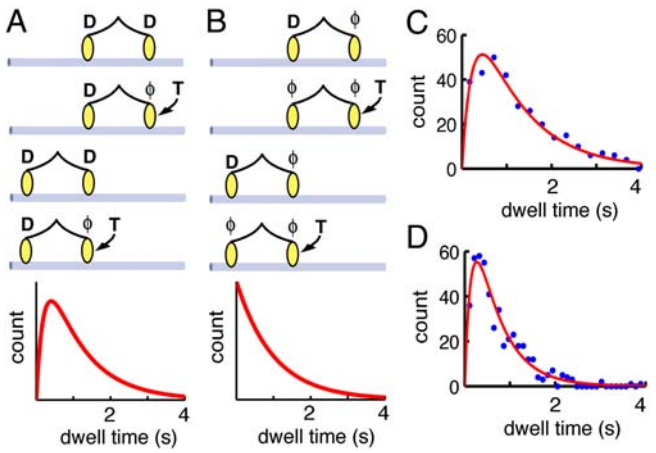

Fig. 4. Intramolecular strain blocks ADP release in the front head of dimeric myosin VI. (*A*) Mechanism with ADP gating. Myosin VI walks right to left. Both ADP release (D; *First Line*) and ATP binding (T; *Second Line*) in the rear head precede the step. ADP release is blocked in the new lead head (*Third Line*). ADP release and ATP binding at the rear head again precede the next step (*Fourth Line*). The resulting dwell time distribution fits a sequential exponential model, with two rates reflecting the rates of rear head ADP release and ATP binding. (*B*) Mechanism without gating. ATP binds to the empty rear head (*ϕ*) resulting in a step (*First and Second Lines*). ADP leaves the front head prior to the next step (*Third and Fourth Lines*). The resulting stepping kinetics are single-exponential, and reflect the ATP binding rate. (*C* and *D*) Sequential exponential model fits (*Red*) to dwell time distributions measured for M6dimer under 1.5 pN load in the optical trap (*C*; 100 μM ATP, $N = 320$, fit rates of $4(3.8) \pm 1$ s^{-1} and $1.0(0.94) \pm 0.1$ s^{-1}) and under no load measured using GNT (*D*; 120 μM ATP, $N = 464$, fit rates of $7(5.8) \pm 1$ and $1.7(1.8) \pm 0.1$ s^{-1}). Fit rates are derived from bootstrap analysis and MLE (parentheses). GNT and optical trap dwell time distributions collected in the presence of saturating ATP resolve sequential processes with rates of 5 and ~30 s^{-1}, corresponding to ADP release and the next slowest process in the catalytic cycle (Figs. S4 and S7). The observation of the much faster 30 s^{-1} rate confirms that both assays can resolve the ~5 s^{-1} rate we attribute to ADP release in panels *C* and *D*.

Our data are most easily interpreted by a class of models in which ADP release must occur before ATP can bind at the rear head. Although several models potentially fulfill this requirement (see *SI Text*), the model that most completely and simply accounts for our data is one in which intramolecular strain blocks ADP release in the front head. We estimate an upper bound for the front head ADP release rate of 0.4 s^{-1} based on Monte Carlo simulations (see *SI Text*).

Our data and model are consistent with prior work in which myosin V dwell time data collected in the presence of rate-limiting ATP concentrations were fit to sequential exponential distributions (21, 42). Although it was not appreciated at the time, previously collected optical trap data for myosin VI provide additional evidence in favor of gated ADP release (see Table S2). Importantly, our GNT data suggest that ADP gating is an integral part of the myosin VI catalytic cycle even in the absence of applied load. Our model is qualitatively consistent with the modest deceleration of ADP release seen in single-headed myosin VI molecules under plus-end-directed load (43). However, a larger change in ADP release rate is required to quantitatively explain our experimental results. This discrepancy may stem from a difference in construct lever arm lengths in the two studies. Alternatively, ADP gating may be strongly geometry dependent, such that it occurs optimally in the context of a dimeric molecule.

Our data are apparently at odds with portions of the model proposed by Sweeney et al., wherein ADP release from the front head is not hindered (25). One possible explanation for this apparent discrepancy is that Sweeney et al. draw their conclusions from bulk data in which the data reflect the initial encounter between myosin VI and actin, as opposed to the subsequent processive steps. An alternate explanation is that Sweeney et al. use a fluorophore-derivatized ADP as a probe of nucleotide binding kinetics. Fluorophore-derivatized ATP is known to exhibit altered kinetics as compared to unmodified ATP in studies performed with myosin V (44).

Importantly, Sweeney et al. additionally propose that intramolecular strain blocks ATP binding to the lead head (25). The presence or absence of front-head ATP gating is not readily tested by our measurements. Thus, while blocked ATP binding to the front head (as proposed by Sweeney et al.) is not necessary to explain our data, it is also not inconsistent with our measurements.

Our data are consistent with a recent report in which single-molecule fluorescence studies were interpreted to support a structural model in which the lead head lever arm is held in its prestroke conformation by intramolecular strain (45). Although Reifenberger et al. propose a kinetic model that lacks ADP gating, the strained lead head conformation that they report provides an appealing mechanism for gated ADP release, analogous to previous myosin V models (40, 41).

We additionally measured the dwell time distributions for swivel 1, 2, and 3 at 200 μM ATP using GNT (Fig. S5). Sequential exponential fits to the swivel 2 and 3 dwell time data yield rates consistent with those measured for M6dimer (Table S1). Interestingly, the fit to the swivel 1 data yields rates of $12(9.9) \pm 6$ and $1.5(1.4) \pm 0.1$ s^{-1} (fit rates are derived from bootstrap analysis; MLE value is provided in parentheses). The rate of 12 s^{-1} is unlikely to result from fast ADP release as compared to M6dimer: smTIRF velocity data show that swivel 1 steps are slower, not faster, than M6dimer at saturating ATP (Table 1).

Swivel 1 makes shorter processive runs and takes more backsteps as compared to M6dimer (Table 1). A possible explanation for these observations is that ADP release is only partially blocked in the lead head of swivel 1 due to the disruption of intramolecular tension. In this scenario, premature release of ADP from the front head of swivel 1 would allow its ATP-mediated

dissociation from actin, which would in turn increase the likelihood of both backward steps and complete detachment from the filament. Although considerable caution is warranted given the uncertainty in the fit parameters (see *SI Text*), the stepping kinetics we observe for swivel 1 are likewise consistent with partially disrupted ADP gating in the absence of load.

Fits to the swivel 1 dwell time distribution observed in the optical trap under 1.25 pN of backward load and 225 μM ATP yield ATP binding and ADP release rates that are similar to those of M6dimer (Fig. S6 and Table S2). Swivel 1 stepping kinetics measured at 1.5 mM ATP and 1.2 pN load are likewise consistent with a swivel 1 rear head ADP release rate that is similar to the M6dimer ADP release rate under these conditions (Fig. S7 and Table S2). These data are thus consistent with gated front-head ADP release in the presence of applied load, as in M6dimer.

Discussion

The modest alterations in run length and step size of the swivel constructs observed in the absence of load demonstrate the surprising robustness of the myosin VI processivity to changes in lever arm properties (see below). However, we do observe a marked decrease in swivel 1 step size under applied load. This observation is easiest to interpret using a model in which a stiff lever arm extension provided by at least a portion of the MT is necessary for the production of processive steps that are roughly matched to the actin periodicity in the presence of a backward load. We and others have previously proposed models in which the PT unfolds during processive stepping (24, 33, 46). Mukherjea et al. and Park et al. propose models in which the MT dimerizes immediately after the PT (24, 33), inducing the PT to unfold to achieve the large step sizes observed. The location of our swivel 1 sequence (inserted at Leu^{914}) is early in the region they propose to be a dimerization domain (residues ~900 to ~940). Our swivel 2 and 3 sequences are near the middle (inserted at residue Gln^{931}) and near the end (Arg^{941}) of that sequence, respectively.

In the Spink et al. model (22), PT unfolding is not necessary in order to generate large steps, although it is also not ruled out. Models in which the MT dimerizes must be reconciled with our observation of systematic trends in processive run lengths and backstep probabilities resulting from the inclusion of the swivel sequence at multiple points within the MT (Table 1). Additionally, either or both of the first two swivel constructs would be expected to disrupt the proposed dimerization domain in the proximal part of the MT. Clearly, further work will be necessary to reconcile the extant experimental observations and structural models of the myosin VI tail.

Our model for myosin VI gating is similar to the commonly accepted model for myosin V gating, in which the ADP release rate from the front head is slow relative to that of the rear head (40, 41). As for myosin V, ADP gating likely serves to increase processivity. Given the emerging cellular roles of myosin VI, we speculate that the proposed ADP gating serves to increase the effective affinity of myosin VI for actin in the presence of applied load, thus improving its performance as both a transporter and as a cytoskeletal anchor (47). Our data do not comment on the possible additional presence of blocked ATP binding to the front head (25). It is possible that myosin VI incorporates both ADP gating and ATP gating.

The data for myosin V, M6dimer, swivel 1, and recently reported dimeric myosin VI constructs with artificial lever arms (48) demonstrate that robust processive stepping can be generated by a variety of lever arm structures and stroke geometries. We therefore hypothesize that the evolution of processivity might be simpler than would otherwise be expected when considering the elaborate kinetic mechanisms (49) of extant track motors.

Materials and Methods

Constructs and Protein Purification. M6dimer was made using porcine myosin VI cDNA truncated at Arg^{992} followed by a GCN4 leucine zipper (MKQLEDKVEELLSKNYHLENEVARLKKLVGE), followed immediately by YFP^{21}. Swivels 1, 2, and 3 dimeric constructs were made by inserting the 11 amino acid sequence GGSGGSGGSGG after amino acids Leu^{914}, Gln^{931}, and Arg^{941} in the control M6 dimer construct. Cloning and protein expression were performed following standard procedures (*SI Text*).

Single-Molecule Assays. See *SI Text* for detailed protocols. Actin and biotinylated actin were prepared using minor variations on established protocols. Single-molecule TIRF microscopy and optical trapping assays were performed as previously described (48, 50). GNT assays used goat anti-rabbit antibody coated 40 nm gold nanoparticles (Ted Pella, Inc.) conjugated to polyclonal rabbit anti-GFP (gift from Aaron Straight, Stanford University). The flow cell was passivated using biotinylated PEG-polylysine branch copolymer (Surface-Solutions Ltd.). Actin adheres weakly to the coverslip surface under these conditions, allowing robust myosin VI processivity.

Data Analysis. Step positions were determined both manually and using the semiautomated method reported by Kerssemakers et al. (51) (*SI Text*). The stroke sizes for monomeric constructs were corrected for mechanical compliances using established techniques (*SI Text*) (46, 52). Run length distributions for runs of length >150 nm were fit to a single-exponential distribution. Cumulative dwell time distributions were fit to the sequential exponential model:

$$F = \left[\frac{k_1}{k_1 - k_2}\exp(-k_2 t) - \frac{k_2}{k_1 - k_2}\exp(-k_1 t)\right]$$

Where k_1 and k_2 are the rates of ADP release and ATP binding, and F is the fraction of dwells of length t or longer. We also histogrammed the data and fit it to the equation:

$$H = \frac{k_1 k_2}{k_1 - k_2}[\exp(-k_2 t) - \exp(-k_1 t)]$$

Here H is the normalized distribution of dwell times. In both cases fit values and errors where determined using the bootstrap method, and confirmed by calculating the maximum likelihood estimates for k_1 and k_2.

Monte Carlo Simulations. We performed Monte Carlo simulations to estimate front-head ADP release rates that are consistent with our observed stepping kinetics (*SI Text*).

ACKNOWLEDGMENTS. The authors thank S. Sivaramakrishnan, M. Elting, and J. Sung for useful discussions and technical assistance. A.R.D. was supported by an American Heart Association postdoctoral fellowship and holds a Career Award at the Scientific Interface from the Burroughs Wellcome Fund. P.C. was supported by A*STAR, Singapore, Z.B. was supported by National Institutes of Health (NIH) Grant DP2 OD004690, and J.A.S. was supported by NIH Grant GM33289 and Human Frontier Science Program Grant GP0054/2009.

1. Wells AL, et al. (1999) Myosin VI is an actin-based motor that moves backwards. *Nature* 401:505–508.
2. Bryant Z, Altman D, Spudich JA (2007) The power stroke of myosin VI and the basis of reverse directionality. *Proc Natl Acad Sci USA* 104:772–777.
3. Ménétrey J, et al. (2005) The structure of the myosin VI motor reveals the mechanism of directionality reversal. *Nature* 435:779–785.
4. Buss F, Kendrick-Jones J (2008) How are the cellular functions of myosin VI regulated within the cell? *Biochem Biophys Res Commun* 369:165–175.
5. Inoue T, et al. (2008) BREK/LMTK2 is a myosin VI-binding protein involved in endosomal membrane trafficking. *Genes Cells* 13:483–495.
6. Chibalina MV, Seaman MN, Miller CC, Kendrick-Jones J, Buss F (2007) Myosin VI and its interacting protein LMTK2 regulate tubule formation and transport to the endocytic recycling compartment. *J Cell Sci* 120:4278–4288.
7. Altman D, Goswami D, Hasson T, Spudich JA, Mayor S (2007) Precise positioning of myosin VI on endocytic vesicles *in vivo*. *PLoS Biol* 5:e210.
8. Spudich G, et al. (2007) Myosin VI targeting to clathrin-coated structures and dimerization is mediated by binding to Disabled-2 and PtdIns(4,5)P2. *Nat Cell Biol* 9:176–183.
9. Osterweil E, Wells DG, Mooseker MS (2005) A role for myosin VI in postsynaptic structure and glutamate receptor endocytosis. *J Cell Biol* 168:329–338.

10. Buss F, et al. (1998) The localization of myosin VI at the golgi complex and leading edge of fibroblasts and its phosphorylation and recruitment into membrane ruffles of A431 cells after growth factor stimulation. *J Cell Biol* 143:1535–1545.
11. Morris SM, et al. (2002) Myosin VI binds to and localises with Dab2, potentially linking receptor-mediated endocytosis and the actin cytoskeleton. *Traffic* 3:331–341.
12. Geisbrecht ER, Montell DJ (2002) Myosin VI is required for E-cadherin-mediated border cell migration. *Nat Cell Biol* 4:616–620.
13. Lin HP, et al. (2007) Cell adhesion molecule Echinoid associates with unconventional myosin VI/Jaguar motor to regulate cell morphology during dorsal closure in Drosophila. *Dev Biol* 311:423–433.
14. Yoshida H, et al. (2004) Lessons from border cell migration in the Drosophila ovary: A role for myosin VI in dissemination of human ovarian cancer. *Proc Natl Acad Sci USA* 101:8144–8149.
15. Wei S, Dunn TA, Isaacs WB, De Marzo AM, Luo J (2008) GOLPH2 and MYO6: Putative prostate cancer markers localized to the Golgi apparatus. *Prostate* 68:1387–1395.
16. Sahlender DA, et al. (2005) Optineurin links myosin VI to the Golgi complex and is involved in Golgi organization and exocytosis. *J Cell Biol* 169:285–295.
17. Heintzelman MB, Hasson T, Mooseker MS (1994) Multiple unconventional myosin domains of the intestinal brush border cytoskeleton. *J Cell Sci* 107:3535–3543.
18. Yang LE, Maunsbach AB, Leong PK, McDonough AA (2005) Redistribution of myosin VI from top to base of proximal tubule microvilli during acute hypertension. *J Am Soc Nephrol* 10:2890–2896.
19. Hertzano R, et al. (2008) A Myo6 mutation destroys coordination between the myosin heads, revealing new functions of myosin VI in the stereocilia of mammalian inner ear hair cells. *PLoS Genet* 4:e1000207.
20. Avraham KB, et al. (1995) The mouse Snell's waltzer deafness gene encodes an unconventional myosin required for structural integrity of inner ear hair cells. *Nat Genet* 11:369–375.
21. Altman D, Sweeney HL, Spudich JA (2004) The mechanism of myosin VI translocation and its load-induced anchoring. *Cell* 116:737–749.
22. Spink BJ, Sivaramakrishnan S, Lipfert J, Doniach S, Spudich JA (2008) Long single alpha-helical tail domains bridge the gap between structure and function of myosin VI. *Nat Struct Mol Biol* 15:591–597.
23. Sivaramakrishnan S, Spink BJ, Sim AY, Doniach S, Spudich JA (2008) Dynamic charge interactions create surprising rigidity in the ER/K alpha-helical protein motif. *Proc Natl Acad Sci USA* 105:13356–13361.
24. Mukherjea M, et al. (2009) Myosin VI dimerization triggers an unfolding of a three-helix bundle in order to extend its reach. *Mol Cell* 35:305–315.
25. Sweeney HL, et al. (2007) How myosin VI coordinates its heads during processive movement. *EMBO J* 26:2682–2692.
26. Yildiz A, et al. (2003) Myosin V walks hand-over-hand: Single fluorophore imaging with 1.5-nm localization. *Science* 300:2061–2065.
27. Dunn AR, Spudich JA (2007) Dynamics of the unbound head during myosin V processive translocation. *Nat Struct Mol Biol* 14:246–248.
28. Yasuda R, Noji H, Yoshida M, Kinosita K, Jr, Itoh H (2001) Resolution of distinct rotational substeps by submillisecond kinetic analysis of F1-ATPase. *Nature* 410:898–904.
29. Braslavsky I, et al. (2001) Objective-type dark-field illumination for scattering from microbeads. *Appl Opt* 40:5650–5657.
30. Nan X, Sims PA, Xie XS (2008) Organelle tracking in a living cell with microsecond time resolution and nanometer spatial precision. *Chemphyschem* 9:707–712.
31. Yildiz A, et al. (2004) Myosin VI steps via a hand-over-hand mechanism with its lever arm undergoing fluctuations when attached to actin. *J Biol Chem* 279:37223–37226.
32. Balci H, Ha T, Sweeney HL, Selvin PR (2005) Interhead distance measurements in myosin VI via SHRImP support a simplified hand-over-hand model. *Biophys J* 89:413–417.
33. Park H, et al. (2006) Full-length myosin VI dimerizes and moves processively along actin filaments upon monomer clustering. *Mol Cell* 21:331–336.
34. Sun Y, et al. (2007) Myosin VI walks "wiggly" on actin with large and variable tilting. *Mol Cell* 28:954–964.
35. De La Cruz EM, Ostap EM, Sweeney HL (2001) Kinetic mechanism and regulation of myosin VI. *J Biol Chem* 276:32373–32381.
36. Ökten Z, Churchman LS, Rock RS, Spudich JA (2004) Myosin VI walks hand-over-hand along actin. *Nat Struct Mol Biol* 11:884–887.
37. Rock RS, et al. (2001) Myosin VI is a processive motor with a large step size. *Proc Natl Acad Sci USA* 98:13655–13659.
38. Sakamoto T, Yildez A, Selvin PR, Sellers JR (2005) Step-size is determined by neck length in myosin V. *Biochemistry* 44:16203–16210.
39. Vilfan A (2005) Elastic lever-arm model for myosin V. *Biophys J* 88:3792–3805.
40. Purcell TJ, Sweeney HL, Spudich JA (2005) A force-dependent state controls the coordination of processive myosin V. *Proc Natl Acad Sci USA* 102:13873–13878.
41. Veigel C, Schmitz S, Wang F, Sellers JR (2005) Load-dependent kinetics of myosin-V can explain its high processivity. *Nat Cell Biol* 7:861–869.
42. Rief M, et al. (2000) Myosin-V stepping kinetics: A molecular model for processivity. *Proc Natl Acad Sci USA* 97:9482–9486.
43. Oguchi Y, et al. (2008) Load-dependent ADP binding to myosins V and VI: Implications for subunit coordination and function. *Proc Natl Acad Sci USA* 105:7714–7719.
44. Sakamoto T, Webb MR, Forgacs E, White HD, Sellers JR (2008) Direct observation of the mechanochemical coupling in myosin Va during processive movement. *Nature* 455:128–132.
45. Reifenberger JG, et al. (2009) Myosin VI undergoes a 180° power stroke implying an uncoupling of the front lever arm. *Proc Natl Acad Sci USA* 106:18255–18260.
46. Rock RS, et al. (2005) A flexible domain is essential for the large step size and processivity of myosin VI. *Mol Cell* 17:603–609.
47. Laakso JM, Lewis JH, Shuman H, Ostap EM (2008) Myosin I can act as a molecular force sensor. *Science* 321:133–136.
48. Liao JC, Elting MW, Delp SL, Spudich JA, Bryant Z (2009) Engineered myosin VI motors reveal minimal structural determinants of directionality and processivity. *J Mol Biol* 392:862–867.
49. Vilfan A (2009) Five models for myosin V. *Front Biosci* 14:2269–2284.
50. Rock RS, Rief M, Mehta AD, Spudich JA (2000) In vitro assays of processive myosin motors. *Methods* 22:373–381.
51. Kerssemakers JW, et al. (2006) Assembly dynamics of microtubules at molecular resolution. *Nature* 442:709–712.
52. Mehta AD, Finer JT, Spudich JA (1997) Detection of single-molecule interactions using correlated thermal diffusion. *Proc Natl Acad Sci USA* 94:7927–7931.